Science AAAS

www.sciencemag.org/cgi/content/full/339/6118/436/DC1

Supplementary Materials for

Synchronous X-ray and Radio Mode Switches: A Rapid Global Transformation of the Pulsar Magnetosphere

W. Hermsen,* J. W. T. Hessels, L. Kuiper, J. van Leeuwen, D. Mitra, J. de Plaa, J. M. Rankin, B. W. Stappers, G. A. E. Wright, R. Basu, A. Alexov, T. Coenen, J.-M. Grießmeier, T. E. Hassall, A. Karastergiou, E. Keane, V. I. Kondratiev, M. Kramer, M. Kuniyoshi, A. Noutsos, M. Serylak, M. Pilia, C. Sobey, P. Weltevrede, K. Zagkouris, A. Asgekar, I. M. Avruch, F. Batejat, M. E. Bell, M. R. Bell, M. J. Bentum, G. Bernardi, P. Best, L. Bîrzan, A. Bonafede, F. Breitling, J. Broderick, M. Brüggen, H. R. Butcher, B. Ciardi, S. Duscha, J. Eislöffel, H. Falcke, R. Fender, C. Ferrari, W. Frieswijk, M. A. Garrett, F. de Gasperin, E. de Geus, A. W. Gunst, G. Heald, M. Hoeft, A. Horneffer, M. Iacobelli, G. Kuper, P. Maat, G. Macario, S. Markoff, J. P. McKean, M. Mevius, J. C. A. Miller-Jones, R. Morganti, H. Munk, E. Orrú, H. Paas, M. Pandey-Pommier, V. N. Pandey, R. Pizzo, A. G. Polatidis, S. Rawlings, W. Reich, H. Röttgering, A. M. M. Scaife, A. Schoenmakers, A. Shulevski, J. Sluman, M. Steinmetz, M. Tagger, Y. Tang, C. Tasse, S. ter Veen, R. Vermeulen, R. H. van de Brink, R. J. van Weeren, R. A. M. J. Wijers, M. W. Wise, O. Wucknitz, S. Yatawatta, P. Zarka

*To whom correspondence should be addressed. E-mail: w.hermsen@sron.nl

Published 25 January 2013, *Science* **339**, 436 (2013)
DOI: 10.1126/science.1230960

This PDF file includes:

Materials and Methods

XMM-Newton observations

Between 4 November and 4 December 2011 we were awarded six XMM-Newton observations (identifiers #1-#6) of about 6 hours duration each in the energy band 0.2 - 10 keV. Table S1 lists the effective exposure times and instrumental setup of the simultaneously used CCD detectors of the European Photon Imaging Camera (EPIC): the PN (*18*) and the MOS-1+2 detectors (*19*). These observations were performed simultaneously with the GMRT at 320 MHz and LOFAR at 140 MHz, firstly to guarantee that we would recognize all abrupt (on time scales of seconds) radio mode changes, but also to be able to study the timing, spectral and polarization characteristics of PSR B0943+10 during the X-ray observations. We did not use the last XMM-Newton observation, which suffered from many solar soft proton flares, resulting in a high background.

GMRT setup and mode determinations

The observations with the GMRT, located near Pune in India, were conducted in the same way as an earlier 8-hour session (*35*) using 20 of the 30 antennas, 14 in the central square and 2 each in the three arms, for ease and stability of the phasing. Short interruptions of the PSR B0943+10 observations were needed every 2-3 hours for re-phasing on a continuum radio source. The array was first phased on the flux calibrator 3C147 and then slewed to a phase calibrator 0837–198 and 1021+216 close to PSR B0943+10 to check for phase stability and re-phasing as required. A bandwidth of 33.33 MHz was used (limits 306 - 339.33 MHz) and the data were recorded using the pulsar mode of the GMRT software backend (*36*) at a time resolution of 0.98304 ms split into 256 channels. After de-dispersion, sections of the data with baseline variations due to broad band interference were mitigated using running mean subtraction as well as flattening of the baseline on a pulse-to-pulse basis. Displays of the processed observations in short averages then provided the needed modal transition times. Figure 1, panel C (in main text) shows an example of a Q- to B-mode transition measured with the GMRT at 320 MHz. In this figure, the disappearance of the weak precursor in the B-mode after the transition is clearly visible.

LOFAR setup and mode determinations

The LOFAR data were acquired by combining the 12 most centrally located high-band antenna sub-stations (the 'Superterp' HBAs, Fig. 1 in (*37*)) located in Exloo, The Netherlands. These 12 sub-stations receive the same clock signal, which greatly facilitates the coherent, 'in phase', addition of their signals. A coherent beam was formed on the position of PSR B0943+10 and tracked throughout the observation. A second beam was formed on nearby pulsar PSR B0950+08 to serve as a reference beam for system sensitivity and radio frequency interference checks. For each beam, the dual-polarization array signal was transformed on-line to the four Stokes parameters. These were sampled every 0.32 ms, for a total bandwidth of 46.875 MHz split into 3840 channels (*38*).

For each of the 6 epochs, the data were folded with an ephemeris from the Jodrell Bank long-term timing program (*17*). Per 1-minute sub-integration, the profile signal-to-noise ratio was calculated versus time, and compared to the expected LOFAR sensitivity curve. Simultaneously, the pulse profile was plotted versus time and phase (Fig. 1, Panel A). In the intensity plots, mode changes were initially identified by eye. We could see the times of mode switches with an accuracy of a few seconds. However, we determined in 10-second resolution plots the UT times for all mode changes generally to 1-minute accuracy, sufficiently accurate for the selection of the X-ray data. The visual inspection of the intensity plots, and the coincidence testing between the PSR B0943+10 and PSR B0950+08 data, allowed for the flagging of two ~5-min sections of broadband radio frequency interference in 42 hours of data.

Table S2 lists time windows used in this work. In the useful XMM-Newton observations (#1 - #5) the B- and Q-mode each appeared for roughly equal amounts of time.

X-ray spatial analysis

Even though PSR B0943+10 is a weak X-ray source (*14*), our long observations detected it easily. In a detailed spatial analysis, we produced maximum-likelihood-ratio maps, which give in each sky bin the ratio of the likelihood that a source is located in that bin in addition to background (in this case assumed to be a flat background level) over the likelihood that just the background (no source) is present, a test statistic for the presence of a source (3*9*). With this method we clearly detected PSR B0943+10 in each of the five XMM-Newton observations using events from the PN detector, and consistently when selecting events from the MOS-1+2 detectors. Using the sensitive area arfgen-1802 and redistribution matrix rmfgen-1561 (implemented in XMMSAS-20110223-1801-1100 (*40*)) for the XMM-response, the derived flux values ranged from the previously published value (*14*) up to more than twice that value, providing significant evidence for time variability. In the next step we separately analyzed events that arrived in the radio B- and Q-mode time windows (Table S2). The detection significance for a similar exposure is twice as high in the radio Q-mode as in the B-mode, and the count rate is more than a factor two higher in the Q-mode than in the B-mode, shown in Fig. S1 for the PN detector. This provides us with evidence for simultaneous mode switching in the radio and X-ray bands.

X-ray timing analysis.

We searched for pulsations in the X-ray data for events detected during the radio Q-mode, in which we had more than twice the number of source counts detected in the B-mode. In order to maximize our statistics, we selected all events within a radius of 15" from the source position (see Fig. S2) for the PN, MOS-1+2 detectors. We verified that this radius gives the optimum signal-to-noise ratio for the XMM point-spread functions. The event arrival times at the satellite have been converted to arrival times at the Solar System Barycenter adopting our new accurate X-ray source position which has a negligible statistical error and a systematic uncertainty of at most 1". Folding these event arrival times using an updated Jodrell Bank ephemeris (fixed X-ray source location, see Table S3) yielded a 6.6-σ signal adopting the Z_1^2 test (Rayleigh test) and revealed a broad pulse profile (see top panel Fig. 2B). The profile can be fitted equally well with a sinusoid or a flat background with a Gaussian shaped pulse. The latter Gaussian pulse template reaches its maximum at phase 0.98 ± 0.02 with $\sigma = 0.20 \pm 0.05$ and is an excellent fit to the 0.5 - 2 keV pulse shown in Fig. 2. We found that X-ray pulsations were detected significantly only in the 0.5-2 keV energy band: 1.2 σ for 0.2-0.5 keV and 1.9 σ for 2-10 keV.

The X-ray events detected during the radio B-mode do not show any evidence for a pulsed signal (1.2 σ for the integral 0.2-10 keV), as can also be seen in the top panel of Fig. 3A. This is an additional manifestation of X-ray mode switching in a radio pulsar, this time revealed in its X-ray timing properties.

X-ray spectral analyses

We first present the results for the total (i.e. pulsed and un-pulsed) X-ray emission in the X-ray-bright, radio-quiet Q-mode. We again use the maximum-likelihood analysis, applying this to the two-dimensional counts sky maps in different energy bins measured with the EPIC PN detector and separately to the summed counts maps for EPIC MOS-1+2. The latter maps have only slightly lower statistics than the PN counts maps and give independent results. The maximum likelihood analysis delivers a count(-rate) spectrum, which can be de-convolved assuming different source input spectra in model fitting. An additional important parameter is the hydrogen column density in the source direction (N_H), causing significant absorption below 2 keV. We fixed N_H at 4.3×10^{20} cm^{-2} for all model fits, the value used in the first study of PSR B0943+10 (*14*). We verified that N_H values reported in the literature, differing by up to ~35 %, influenced the model-fit parameters only within their 1σ uncertainties.

Figure 3A shows the unabsorbed (i.e. corrected for absorption by the hydrogen column density) total X-ray photon spectrum in the radio Q-mode. The filled symbols are the flux values for the PN data and the open symbols for the MOS-1+2 data. The best model fitted to both sets of flux values simultaneously is the sum of a component with a power-law shape (broken line) and one with a BB-shape (dotted line). This fit was an improvement at the 4.1 σ level with respect to a fit with a single PL, and 3.5 σ relative to a single BB-model fit. All spectral parameters for the three model fits (BB+PL, BB, PL) are given in Table S4. The contributions of the two components in the X-ray band 0.5 - 8 keV are equal, each ~7.5×10^{15} erg cm^{-2} s^{-1}, to be compared with the value of $4.4^{+1.8}_{-1.5} \times 10^{-15}$ erg cm^{-2} s^{-1} reported in the first detection (*14*) for a PL fit to the total spectrum with the same index $\Gamma=2.6^{+0.7}_{-0.5}$. This suggests that in this early observation of 20-ks duration PSR B0943+10 was predominantly in the B-mode, when the X-ray flux is low.

The spectrum of the pulsed component in the Q-mode can be determined by first deriving the pulse excess counts above a flat background level in the pulse profiles for differential energy bins. These excess counts were derived by fitting with the template Gaussian profile derived in the 0.5 - 2 keV energy band (parameters given above). We verified that there is no significant variation in profile shape over the total X-ray band. A single BB model gave an excellent fit, a PL model was acceptable only at the 3% level (main discrepancy at 0.2 - 0.5 keV energies; see also in Table S5 the lack of evidence for pulsed emission below 0.5 keV). Figure 3B shows the reconstructed unabsorbed photon spectrum of the pulsed component with the best fit model superposed. Full details of the two model (BB and PL) fits are given in Table S4.

The spectral parameters of the thermal component in the best fit (PL + BB) to the total Q-mode spectrum and the thermal pulsed spectrum in the Q-mode appear to be statistically consistent (Δ flux is 0.1 σ and ΔkT=2.5 σ). In other words, this means that the Q-mode total X-ray emission consists of an un-pulsed component with a non-thermal PL spectrum, and a pulsed component with a thermal BB spectrum. This is also reflected in the variation of the pulsed fraction with energy (see Table S5). It is important to note that XMM-Newton is very sensitive in the low-energy interval 0.2-0.5 keV, and PSR B0943+10 is detected at a high significance in the sky maps in this energy band, e.g. in just the PN sky map at a level of 12 σ. Therefore, the non-detection of a pulsed signal below 0.5 keV is not due to a lack of sensitivity of XMM-Newton.

Finally, the total X-ray spectrum in the radio B-mode can be derived in analyses of counts sky maps as explained above for the total spectrum in the Q-mode. In this case the counting statistics are low, and it is not possible to discriminate between a single PL and a BB model, both give good fits (Table S4 and Fig. S2). Figure 3C shows the un-pulsed total B-mode spectrum assuming a PL spectrum. We selected this fit for the composite Fig.3, because we find it indicative that the total un-pulsed X-ray emission in the radio B-mode has a spectrum statistically identical to the un-pulsed PL component in the Q-mode (Δ flux is 0.05 σ and $\Delta\Gamma$ is 0.8 σ). This would lead to the conclusion that the mode switching from B- to Q-mode means the addition of a new thermal component consistent with 100% pulsation in the X-ray domain, and no change in the un-pulsed non-thermal component. If one would assume on the other hand, the B-mode un-pulsed X-ray spectrum to be thermal (BB with kT = 0.250±0.006 keV, and flux = 5.36±0.78) 10^{-15} erg $cm^{-2}s^{-1}$, see Table S4), then in the mode switching the un-pulsed thermal component in the B-mode has to be replaced in the Q-mode by an un-pulsed power-law component and, in addition, a new pulsed thermal component has to be added. We consider the first interpretation of the B-mode spectrum most likely.

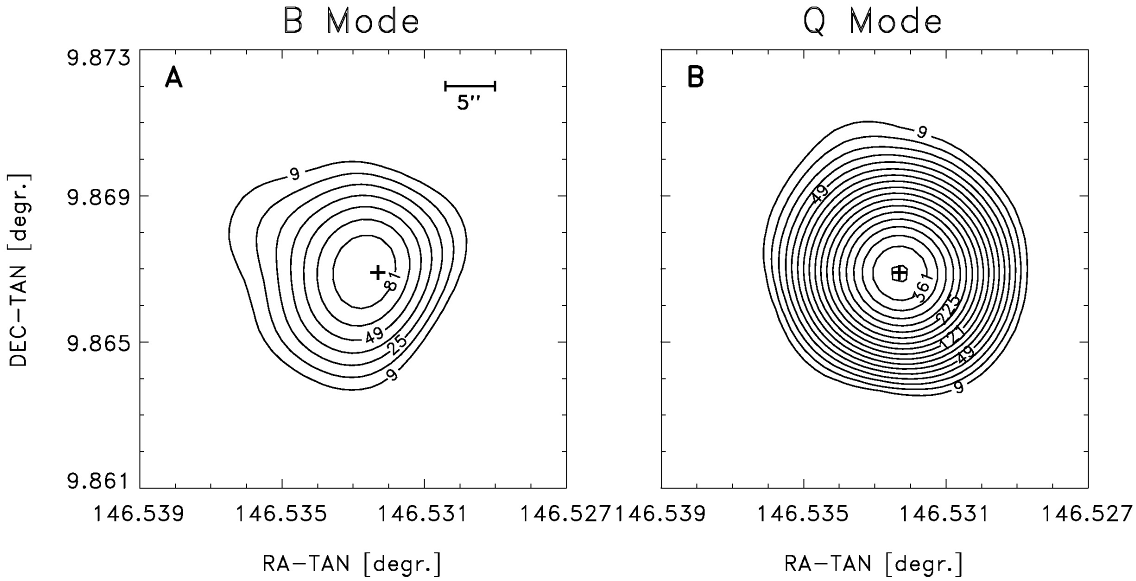

Fig. S1. Maximum-likelihood-ratio sky maps for X-ray energies 0.2-10 keV showing evidence for the detection of PSR B0943+10 with the PN CCDs aboard XMM-Newton in the two radio-defined modes. Panel A: for events selected in the radio B-mode time windows a 9.9 σ detection significance and count rate $(0.44 \pm 0.07)\mathrm{x}10^{-2}$ counts/s. Panel B: for events in the radio Q-mode a 20 σ detection and more than twice the count rate (1.08 ± 0.08) 10^{-2} counts/s. The contour values give the variance of the detection significances in number of σ's, assuming one degree of freedom. The + symbol gives the best location for PSR B0943+10 derived from these XMM-Newton observations (see Table S3).

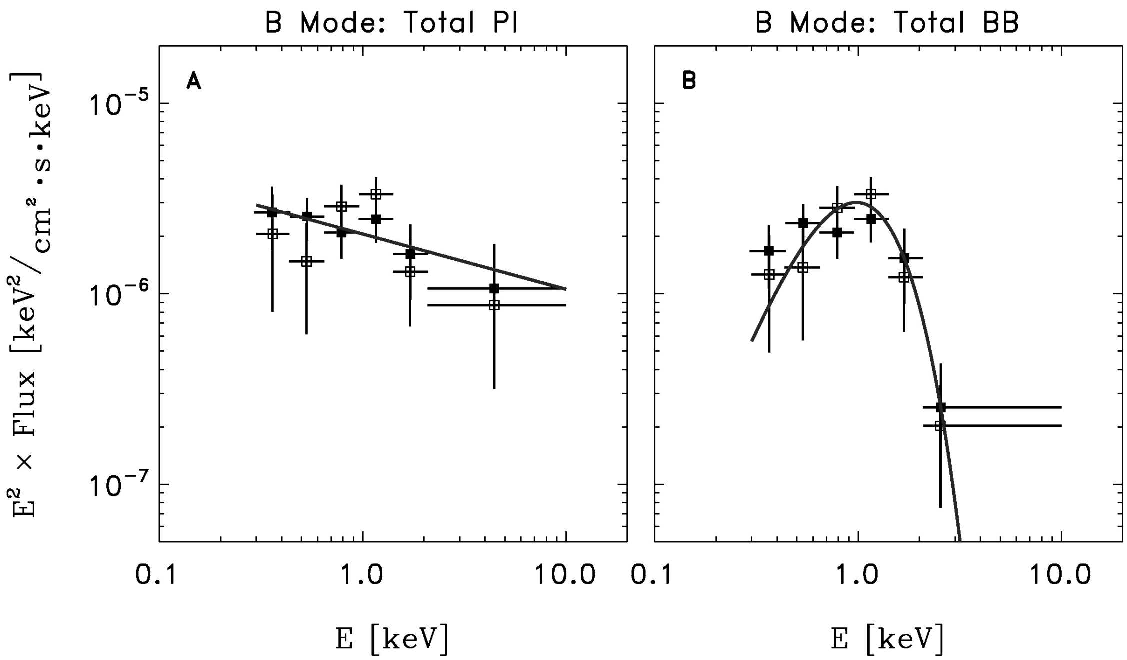

Fig. S2. Unabsorbed total (i.e. pulsed and un-pulsed) X-ray photon spectra of PSR B0943+10 from spatial analyses of events selected in the radio B-mode time windows for the XMM EPIC PN CCDs (filled symbols) and MOS1+2 CCDs (open symbols). Panel A: flux values assuming an underlying PL source spectrum, the solid line show the best fit. Panel B: flux values for a BB spectrum, the solid line shows the best thermal fit. Note: the measured count rates are the same for both figures, but the de-convolved flux values depend on the assumed source spectrum. Both spectral shapes give equally good fits to the measured count-rate spectra (see Table S4).

Table S1. XMM-Newton effective (corrected for dead time) observation times (kilo seconds) in November and December 2011 for the PN, MOS-1 and MOS-2 CCDs of EPIC. The first row gives the observation identifier and day. The selected detector modes, indicated in the last column, allow spatial and pulsar-timing studies. Observation #6 suffered from too many solar proton flares and has not been used in this work.

OBSID, date (day/month)/ CCDs	**#1 4/11**	**#2 6/11**	**#3 21-22/11**	**#4 27-28/11**	**#5 1-2/12**	**#6 4/12**	**Detector mode**
EPIC PN	15.3	24.2	23.0	20.7	20.8	19.0	Full Frame
EPIC MOS-1	21.7	25.9	24.7	22.3	22.5	20.7	Small Window
EPIC MOS-2	21.7	25.9	24.7	22.4	22.5	20.7	Small Window

Table S2. B- and Q-mode time windows identified in both our GMRT and LOFAR observations, covering completely our XMM-Newton observations with observation identifiers (OBSID) #1 to #5. The last column marks the UTC start and end times of individual B- and Q- modes with an accuracy of a minute, sufficiently accurate for the X-ray selections.

XMM OBSID	**Radio mode**	**Day**	**Start - end UTC**
#1	Q	2011-11-04	00:55 - 01:45
	B	2011-11-04	01:45 - 05:35
	Q	2011-11-04	05:35 - 06:03
	B	2011-11-04	06:03 - 07:25
#2	Q	2011-11-06	00:55 - 07:10
	B	2011-11-06	07:10 - 08:35
#3	Q	2011-11-21	23:30 - 06:10
	B	2011-11-22	06:10 - 07:00
#4	Q	2011-11-27	23:30 - 02:40
	B	2011-11-28	02:40 - 06:15
#5	Q	2011-12-01	23:00 - 01:53
	B	2011-12-02	01:53 - 06:00

Table S3. Jodrell Bank ephemeris of PSR B0943+10 valid during our XMM-Newton observations with the improved source position from our X-ray observations.

α_{2000}	$09^h\ 46^m\ 7^s.787$
δ_{2000}	09^o 52' 0''.76
Epoch (TDB)	54226
ν	0.910989538329 Hz
$d\nu/dt$	-2.94219×10^{-15} Hz s^{-1}
$d^2\nu/dt^2$	-1.39×10^{-25} Hz s^{-2}
Start (MJD)	52573
End (MJD)	55880
Solar System Ephem.	DE200

Table S4. Spectral parameters with 1σ errors for the best model fits to the X-ray spectra for: i) the radio Q-mode windows of the total emission measured in the sky map, ii) the radio Q-mode of the pulsed emission measured in the pulse profiles, and iii) the radio B-mode windows of the total emission. The model spectra are black body (BB), power law (PL); the normalization of the PL is at 1 keV. The column density N_H has been fixed at 4.3×10^{20} cm^{-2}. The unabsorbed fluxes (F) and isotropic luminosities (L) for the BB and PL components are calculated for the energy interval 0.5 - 8 keV and a source distance of 630 pc.

Mode **total / pulsed**	Q total	Q total	Q total	Q pulsed	Q pulsed	B total	B total
Model	BB+PL	BB	PL	BB	PL	BB	PL
BB_{norm} x 10^4	1.44±0.27	3.94 ± 0.23		0.81±0.11		1.61±0.16	
BB (kT) keV	0.277±0.012	0.249±0.003		0.319±0.012		0.250±0.006	
PL_{norm} x 10^6	2.30±0.49		4.74±0.27		2.47±0.37		2.06±0.21
PL, Γ ($\alpha E^{-\Gamma}$)	2.60±0.34		2.44±0.08		1.97±0.18		2.29±0.16
F_{BB} x 10^{15} erg cm^{-2} s^{-1} unabsorbed	7.52±2.20	12.88±1.01		7.81±1.64		5.36±0.78	
L_{BB} 10^{29} erg s^{-1}	3.6±1.0	6.1±0.5		3.7±0.8		2.5±0.4	
F_{PL} x 10^{15} erg cm^{-2} s^{-1} unabsorbed	7.55±1.81		16.49±1.10		11.21±2.21		7.69±1.00
L_{PL} 10^{29} erg s^{-1}	3.6±0.9		7.9±0.5		5.3±1.1		3.7±0.5
χ^2_{red} / dof	0.81 / 20	1.44 / 22	1.67 / 22	0.38 / 3	3.17 / 3	0.88 / 10	0.74 / 10

Table S5. Pulsed fractions of PSR B0943+10, when the pulsar is in the radio Q-mode, as a function of energy, defined as the ratio of the integrated flux in the pulse profile over the total (i.e. pulsed and un-pulsed) flux of the point source measured in the sky maps. Errors are 1 σ.

Energy interval keV	Pulsed fraction
0.2 - 0.5	0.10 ± 0.15
0.5 - 0.8	0.44 ± 0.16
0.8 - 1.3	0.62 ± 0.14
1.3 - 2.0	0.60 ± 0.17
2.0 - 10	0.72 ± 0.53

References

1. M. Ruderman, P. Sutherland, Theory of pulsars—Polar caps, sparks, and coherent microwave radiation. *Astrophys. J.* **196**, 51 (1975). doi:10.1086/153393

2. J. Arons, E. T. Scharlemann, Pair formation above pulsar polar caps—Structure of the low altitude acceleration zone. *Astrophys. J.* **231**, 854 (1979). doi:10.1086/157250

3. D. C. Backer, Pulsar nulling phenomena. *Nature* **228**, 42 (1970). doi:10.1038/228042a0 Medline

4. K. H. Hesse, R. Wielebinski, *Astron. Astrophys.* **31**, 409 (1974).

5. M. Kramer, A. G. Lyne, J. T. O'Brien, C. A. Jordan, D. R. Lorimer, A periodically active pulsar giving insight into magnetospheric physics. *Science* **312**, 549 (2006). doi:10.1126/science.1124060 Medline

6. F. Camilo, S. M. Ransom, S. Chatterjee, S. Johnston, P. Demorest, PSR J1841-0500: A radio pulsar that mostly is not there. *Astrophys. J.* **746**, 63 (2012). doi:10.1088/0004-637X/746/1/63

7. D. R. Lorimer *et al.*, Radio and x-ray observations of the intermittent pulsar J1832+0029. *Astrophys. J.* **758**, 141 (2012). doi:10.1088/0004-637X/758/2/141

8. A. Lyne, G. Hobbs, M. Kramer, I. Stairs, B. W. Stappers, Switched magnetospheric regulation of pulsar spin-down. *Science* **329**, 408 (2010). doi:10.1126/science.1186683 Medline

9. A. A. Abdo *et al.*, The first Fermi Large Area Telescope catalog of gamma-ray pulsars. *Astrophys. J. Suppl. Ser.* **187**, 460 (2010). doi:10.1088/0067-0049/187/2/460

10. A. Shearer *et al.*, Enhanced optical emission during Crab giant radio pulses. *Science* **301**, 493 (2003). doi:10.1126/science.1084919 Medline

11. S. A. Suleymanova, V. A. Izvekova, *Sov. Astron.* **28**, 32 (1984).

12. J. M. Rankin, S. A. Suleymanova, The topology and polarisation of subbeams associated with the "drifting" subpulse emission of pulsar B0943+10. *Astron. Astrophys.* **453**, 679 (2006). doi:10.1051/0004-6361:20054140

13. I. Backus, D. Mitra, J. Rankin, *Mon. Not. R. Astron. Soc.* **404**, 30 (2010).

14. B. Zhang, D. Sanwal, G. G. Pavlov, An XMM-Newton observation of the drifting pulsar B0943+10. *Astrophys. J.* **624**, L109 (2005). doi:10.1086/430522

15. J. Gil, G. Melikidze, B. Zhang, Formation of a partially screened inner acceleration region in radio pulsars: Drifting subpulses and thermal x-ray emission from polar cap surface. *Astrophys. J.* **650**, 1048 (2006). doi:10.1086/506982

16. See supplementary materials on *Science* Online.

17. G. Hobbs, A. G. Lyne, M. Kramer, C. E. Martin, C. Jordan, Long-term timing observations of 374 pulsars. *Mon. Not. R. Astron. Soc.* **353**, 1311 (2004). doi:10.1111/j.1365-2966.2004.08157.x

18. L. Strüder *et al.*, The European Photon Imaging Camera on XMM-Newton: The PN-CCD camera. *Astron. Astrophys.* **365**, L18 (2001). doi:10.1051/0004-6361:20000066

19. M. J. L. Turner *et al.*, The European Photon Imaging Camera on XMM-Newton: The MOS cameras. *Astron. Astrophys.* **365**, L27 (2001). doi:10.1051/0004-6361:20000087

20. W. Becker *et al.*, Revealing the x-ray emission processes of old rotation-powered pulsars: XMM-Newton observations of PSR B0950+08, PSR B0823+26, and PSR J2043+2740. *Astrophys. J.* **615**, 908 (2004). doi:10.1086/424498

21. J. Gil *et al.*, XMM-Newton observations of radio pulsars B0834+06 and B0826−34 and implications for the pulsar inner accelerator. *Astrophys. J.* **686**, 497 (2008). doi:10.1086/590657

22. W. W. Zhu *et al.*, Chandra observations of the high-magnetic-field radio pulsar J1718–3718. *Astrophys. J.* **734**, 44 (2011). doi:10.1088/0004-637X/734/1/44

23. J. Gil, M. Sendyk, Spark model for pulsar radiation modulation patterns. *Astrophys. J.* **541**, 351 (2000). doi:10.1086/309394

24. A. A. Deshpande, J. M. Rankin, The topology and polarization of sub-beams associated with the ‘drifting’ sub-pulse emission of pulsar B0943+10—I. Analysis of Arecibo 430- and 111-MHz observations. *Mon. Not. R. Astron. Soc.* **322**, 438 (2001). doi:10.1046/j.1365-8711.2001.04079.x

25. A. K. Harding, A. G. Muslimov, Pulsar polar cap heating and surface thermal x-ray emission. II. Inverse Compton radiation pair fronts. *Astrophys. J.* **568**, 862 (2002). doi:10.1086/338985

26. B. Zhang, A. K. Harding, Full polar cap cascade scenario: Gamma-ray and x-ray luminosities from spin-powered pulsars. *Astrophys. J.* **532**, 1150 (2000). doi:10.1086/308598

27. J. M. Rankin, Toward an empirical theory of pulsar emission. VI—The geometry of the conal emission region: Appendix and tables. *Astrophys. J.* **405**, 285 (1993).

28. M. Lyutikov, C. Thompson, Magnetospheric eclipses in the double pulsar system PSR J0737−3039. *Astrophys. J.* **634**, 1223 (2005). doi:10.1086/432252

29. R. P. Breton *et al.*, The double pulsar eclipses. I. Phenomenology and multi-frequency analysis. *Astrophys. J.* **747**, 89 (2012). doi:10.1088/0004-637X/747/2/89

30. A. N. Timokhin, Time-dependent pair cascades in magnetospheres of neutron stars—I. Dynamics of the polar cap cascade with no particle supply from the neutron star surface. *Mon. Not. R. Astron. Soc.* **408**, L41 (2010). doi:10.1111/j.1365-2966.2010.17286.x

31. B. Zhang, G. J. Qiao, W. P. Lin, J. L. Han, Three modes of pulsar inner gap. *Astrophys. J.* **478**, 313 (1997). doi:10.1086/303787

32. S. P. Goodwin, J. Mestel, L. Mestel, G. A. E. Wright, An idealized pulsar magnetosphere: The relativistic force-free approximation. *Mon. Not. R. Astron. Soc.* **349**, 213 (2004). doi:10.1111/j.1365-2966.2004.07481.x

33. A. N. Timokhin, On the force-free magnetosphere of an aligned rotator. *Mon. Not. R. Astron. Soc.* **368**, 1055 (2006). doi:10.1111/j.1365-2966.2006.10192.x

34. J. M. Rankin, Toward an empirical theory of pulsar emission. III—Mode changing, drifting subpulses, and pulse nulling. *Astrophys. J.* **301**, 901 (1986). doi:10.1086/163955

35. I. Backus, D. Mitra, J. Rankin, The topology and polarization of subbeams associated with the 'drifting' subpulse emission of pulsar B0943+10—VI. Analysis of an 8-h Giant Metrewave Radio Telescope observation. *Mon. Not. R. Astron. Soc.* **418**, 1736 (2011). doi:10.1111/j.1365-2966.2011.19595.x

36. J. Roy *et al.*, A real-time software backend for the GMRT. *Exp. Astron.* **28**, 25 (2010). doi:10.1007/s10686-010-9187-0

37. B. W. Stappers *et al*., Observing pulsars and fast transients with LOFAR. *Astron. Astrophys.* **530**, A80 (2011). doi:10.1051/0004-6361/201116681

38. A. Alexov, J. Hessels, J. D. Mol, B. W. Stappers, J. van Leeuwen, *Astron. Soc. Pac. Conf. Ser.* **434**, 193 (2010).

39. A. M. T. Pollock *et al*., *Astron. Astrophys.* **94**, 116 (1981).

40. XMMSAS-20110223-1801-1100: http://xmm.esac.esa.int/sas/.